A synthesis of upper ocean geostrophic kinetic energy spectra from a global submesoscale permitting simulation

Hemant Khatri[1], Stephen M Griffies[2], Takaya Uchida[3], Han Wang[4], and Dimitris Menemenlis[5]

[1]Princeton University
[2]GFDL, NOAA
[3]Institut des Géosciences de l'Environnement
[4]University of Toronto
[5]Jet Propulsion Laboratory, California Institute of Technology

November 26, 2022

Abstract

A submesoscale-permitting global ocean model is used to study the upper ocean turbulence. Submesoscale processes peak in winter and, consequently, geostrophic kinetic energy (KE) spectra tend to be relatively shallow in winter (k^{-2}) with steeper spectra in summer (k^{-3}). This seasonal transition from steep to shallow power-law in the KE spectra indicates a transition from quasi-geostrophic (QG) turbulence in summer to pronounced surface-QG-like turbulence in winter. It is shown that this transition in KE spectral scaling has two phases. In the first phase (late autumn), KE spectra show a presence of two spectral regimes: k^{-3} scaling in mesoscales (100-300 km) and k^{-2} scaling in submesoscales (<50 km), indicating the coexistence of QG, surface-QG, and frontal dynamics. In the second phase (late winter), mixed-layer instabilities convert available potential energy into KE, which cascades upscale leading to flattening of the KE spectra at larger scales, and k^{-2} power-law develops in mesoscales too.

A synthesis of upper ocean geostrophic kinetic energy spectra from a global submesoscale permitting simulation

Hemant Khatri[1*], Stephen M. Griffies[1,2], Takaya Uchida[3], Han Wang[4], Dimitris Menemenlis[5]

[1]Atmospheric and Oceanic Sciences Program, Princeton University, Princeton, New Jersey, USA
[2]NOAA Geophysical Fluid Dynamics Laboratory, Princeton, New Jersey, USA
[3]Institut des Géosciences de l'Environnment, Centre National de la Recherche Scientifique, Grenoble, France
[4]Department of Physics, University of Toronto, Toronto, Canada
[5]Jet Propulsion Laboratory, California Institute of Technology, Pasadena, California, USA

Key Points:

- Seasonality in the upper ocean turbulence is explained as a combination of QG turbulence, surface-QG turbulence, and frontal dynamics.
- Both k^{-3} and k^{-2} power-laws coexist in the horizontal wavenumber spectrum of geostrophic kinetic energy in late autumn months.
- A wavenumber estimate is derived to predict the transition from the enstrophy-cascading to buoyancy-variance-cascading inertial range.

*Atmospheric and Oceanic Sciences Program, 300 Forrestal Road, Sayre Hall, Princeton, NJ 08540-6654, USA

Corresponding author: Hemant Khatri, `hkhatri@princeton.edu`

Abstract

A submesoscale-permitting global ocean model is used to study the upper ocean turbulence. Submesoscale processes peak in winter and, consequently, geostrophic kinetic energy (KE) spectra tend to be relatively shallow in winter ($\sim k^{-2}$) with steeper spectra in summer ($\sim k^{-3}$). This seasonal transition from steep to shallow power-law in the KE spectra indicates a transition from quasi-geostrophic (QG) turbulence in summer to pronounced surface-QG-like turbulence in winter. It is shown that this transition in KE spectral scaling has two phases. In the first phase (late autumn), KE spectra show a presence of two spectral regimes: $\sim k^{-3}$ scaling in mesoscales ($100 - 300$ km) and $\sim k^{-2}$ scaling in submesoscales (< 50 km), indicating the coexistence of QG, surface-QG, and frontal dynamics. In the second phase (late winter), mixed-layer instabilities convert available potential energy into KE, which cascades upscale leading to flattening of the KE spectra at larger scales, and k^{-2} power-law develops in mesoscales too.

Plain Language Summary

Mesoscale ($100 - 300$ km) and submesoscale ($1 - 50$ km) motions are important for heat and material transport in the oceans. In the upper ocean, submesoscale turbulence shows seasonal variability and is pronounced in winter, whereas mesoscale turbulence has less seasonal variations. The same distinction is reflected in horizontal wavenumber spectra of KE and spectral energy fluxes. In this study, geostrophic KE spectra are analyzed in a submesoscale-permitting global ocean model to study the seasonal variability in the upper ocean turbulence. We interpret the results in terms of different physical mechanisms and their effects on the evolution of KE spectra over an annual cycle. We find that both mesoscale and submesoscale processes contribute to their characterization.

1 Introduction

In the mid-latitudes, ocean flows at length scales of order 100 km or larger are predominantly geostrophic so that the flow is quasi-two-dimensional and the Rossby number is small ($Ro < 1$). Consequently, mesoscale (wavelengths roughly $100 - 300$ km) turbulence is generally in accord with theories of two-dimensional turbulence (Kraichnan, 1967) and quasi-geostrophic (QG) turbulence (Charney, 1971). A key feature of such theories is the prediction of an inverse cascade of kinetic energy (KE) at scales greater than the baroclinic Rossby deformation scale (Gkioulekas & Tung, 2007b). In accord with QG turbulence, numerous studies have observed an upscale (or inverse) transfer of KE at length scales larger than about 200 km in the upper ocean (Aluie et al., 2017; Arbic et al., 2014; Schlösser & Eden, 2007; Scott & Wang, 2005; Tulloch et al., 2011) and a forward (or downscale) transfer of enstrophy at smaller scales accompanied by $\sim k^{-3}$ power-law in KE spectra (Khatri et al., 2018).

In the upper ocean, submesoscale (wavelengths roughly $1 - 50$ km, $Ro \sim 1$) turbulence plays an equally important role in the inter-scale energy transfer with corresponding effects on KE spectra (Capet, McWilliams, et al., 2008a, 2008b). Submesoscale processes such as frontogenesis (Haine & Marshall, 1998; McWilliams et al., 2015) and mixed-layer baroclinic instabilities (Boccaletti et al., 2007; Fox-Kemper et al., 2008) show a significant seasonal variability with the strongest activity in winter (Mensa et al., 2013; Rocha, Gille, et al., 2016; Sasaki et al., 2017). This seasonal variability is reflected in submesoscale KE spectra, which tend to follow k^{-2} power-law in winter and k^{-3} in summer (Callies et al., 2015; Uchida et al., 2017). In fact, spectral scaling in mesoscale KE spectra is also seen to vary between k^{-2} to k^{-3} depending on the region of interest (Wortham & Wunsch, 2014; Xu & Fu, 2012).

It has been hypothesized that wintertime submesoscale dynamics near the ocean surface agree with surface-QG turbulence. In a surface-QG regime, buoyancy variance cascades downscale, which in turn leads to $k^{-5/3}$ power-law in potential energy (PE) and KE spectra (Blumen, 1978; Held et al., 1995; Lapeyre, 2017; Pierrehumbert et al., 1994; Sukhatme & Pierrehumbert, 2002), while KE is expected to cascade upscale (Capet, Klein, et al., 2008). However, surface-QG theory does not account for secondary ageostrophic motions, which are important in frontogenesis processes (Hoskins & Bretherton, 1972). Surface-QG dynamics support the formation of strong buoyancy gradients, and, if the horizontal advection due to the ageostrophic flow component is considered, asymmetries develop in the divergence field and in the structure of vertical velocity associated with filaments (Badin, 2013; Ragone & Badin, 2016). These asymmetries tend to form discontinuities in velocity and buoyancy fields resulting in the formation of sharp frontal structures. Consequently, k^{-2} spectral scaling (characteristic of a Heaviside step function) develops in geostrophic KE spectra (Boyd, 1992; Callies & Ferrari, 2013; Klein et al., 2008). Nevertheless, a downscale cascade of buoyancy variance is expected (Sukhatme & Smith, 2009). Hence, as we argue in this paper, the k^{-2} scaling in upper ocean submesoscale KE spectra in winter is consistent with surface-QG-like turbulence. To avoid ambiguity, we refer to surface-QG turbulence in the presence of fronts and secondary ageostrophic motions as "frontal-surface-QG turbulence" in the rest of the paper.

On the contrary, an upscale KE transfer due to mixed-layer instabilities can flatten the KE spectrum, as QG theory predicts $k^{-5/3}$ scaling in the inverse KE cascade inertial range (Charney, 1971), and result in $\sim k^{-2}$ scaling at submesoscales in the winter KE spectrum (Boccaletti et al., 2007; Klein et al., 2008). In fact, there is evidence of inverse KE cascade even in the submesoscale range (Capet, McWilliams, et al., 2008b; Dong et al., 2020; Sasaki et al., 2017; Schubert et al., 2020). Note that these interpretations of KE spectra hold for the geostrophically balanced part of the flow field, which is the focus of our study. If the ageostrophic component is considered in the KE spectrum, the presence of gravity waves can result in a k^{-2} spectral scaling at submesoscales (Garrett & Munk, 1975; Rocha, Gille, et al., 2016; Torres et al., 2018). A more detailed discussion of various ocean turbulence theories can be found in Callies and Ferrari (2013).

Submesoscale processes are crucial for ocean heat uptake and material transport (Su et al., 2018; Uchida et al., 2019), and understanding the physics of seasonality in submesoscales is a key to understanding the impacts of submesoscale processes on mesoscale dynamics and the large-scale circulation. Moreover, studying upper-ocean submesoscale dynamics has applications for the upcoming Surface Water and Ocean Topography satellite mission, which aims to provide measurements at submesoscales (Fu & Ubelmann, 2014).

In this study, we characterize how geostrophic turbulence in mesoscales and submesoscales in the ocean surface mixed-layer transitions seasonally from being QG-like in summer to frontal-surface-QG-like in winter. We frame our interpretations according to the following theoretical predictions: for QG turbulence, KE spectra follow k^{-3} scaling associated with the forward enstrophy cascade (Callies & Ferrari, 2013; Charney, 1971); for frontal-surface-QG turbulence, KE spectra follow k^{-2} scaling associated with the forward cascade of buoyancy variance (Blumen, 1978; Boyd, 1992). We use the output from a submesoscale-permitting global ocean model to study the behavior of upper ocean geostrophic turbulence in different parts of the world. Specifically, we analyze the temporal evolution of geostrophic KE spectral slopes, i.e., transition from k^{-3} in summer to k^{-2} to winter. For the first time, we show a simultaneous presence of two power-laws (k^{-3} and k^{-2}) in geostrophic KE spectra, indicating the coexistence of QG and frontal-surface-QG turbulence. Further, we propose a wavenumber estimate to predict the transition point from k^{-3} to k^{-2} scaling. The role of mixed-layer instabilities is also discussed.

The paper is organized as the following. The model details and methods are provided in section 2, with results then presented in sections 3 and 4. We conclude the paper in section 5.

2 Methods

We analyze output from the 14-month (Sept 2011 to Nov 2012) LLC4320 global ocean simulation (1/48° horizontal grid spacing with 90 vertical levels) performed using the Massachusetts Institute of Technology general circulation model (Marshall et al., 1997; Rocha, Gille, et al., 2016). LLC4320 output is appropriate for studying submesoscale processes since the model resolves dynamical processes with length scales as small as 10 km (Rocha, Gille, et al., 2016). LLC4320 output has been employed in several works to study geostrophic dynamics at mesoscales and submesoscales as well as to understand interactions between balanced motions and inertia-gravity waves (Chereskin et al., 2019; Dong et al., 2020; Qiu et al., 2018; Rocha, Chereskin, et al., 2016; Rocha, Gille, et al., 2016; Torres et al., 2018). We use LLC4320 output to study the interplay between mesoscale and submesoscale turbulence in the upper ocean. For this purpose, we analyzed ten $10^\circ \times 10^\circ$ mid-latitude regions away from continental boundaries. Also, the ocean depth is at least 1 km in these regions so that we expect topographic effects to be minimal. Most energetic ocean mesoscale eddies are generally $100-300$ km, so that the $10^\circ \times 10^\circ$ domains are large enough to contain mesoscale turbulence. Five of the regions are in relatively high KE locations, e.g., near the Gulf Stream, Kuroshio Current, and in the Southern Ocean. The other five regions are in relatively low KE locations (see Figure 1). Recently, Sasaki et al. (2017) observed significant differences in the nature of submesoscale turbulence between high and low KE regions in the North Pacific. With our choice of domains, we investigate the nature of mesoscale and submesoscale turbulence in a range of dynamically different locations in the mid-latitudes.

In LLC4320 output, the essential fields are available as hourly snapshots for the entire duration of the simulation. We compute horizontal wavenumber spectra of KE ($\mathbf{u}^2/2$, where $\mathbf{u}$ is the horizontal velocity) and PE ($b^2/2N^2$, b is buoyancy and N is buoyancy frequency) using velocity and density fields at different depths. In particular, we perform a Helmholtz decomposition of the two-dimensional velocity spectra to compute the KE spectra of the rotational and divergent components (Callies & Ferrari, 2013; Bühler et al., 2014; Uchida et al., 2017). For the spectral computations, we use snapshots rather than daily-averaged fields. Although time-averaging is useful in removing high-frequency inertia-gravity waves from the flow field, it can also suppress balanced submesoscale motions, which have typical timescales of $\mathcal{O}(1)$ day (McWilliams, 2016; Uchida et al., 2019). Thus, time-averaging may suppress seasonal variability at submesoscales. Also, spectra obtained from time-averaged fields tend to be relatively steeper than spectra computed using snapshots (see Figure 3 in Sinha et al., 2019). This artifact would compromise our ability to compare spectral slopes against theoretical predictions. We used velocity and density snapshots at 12-hour intervals and at seven vertical levels down to 650 m depth, with seasonally and monthly-averaged spectra examined. Prior to computations, horizontal spatial linear trends were removed from each data snapshot (Uchida et al., 2017) and the Planck-taper windowing function was used to make the fields doubly-periodic (McKechan et al., 2010). We provide further details on the spectra calculations in supporting information.

3 Seasonality in submesoscale KE spectra

Figures 2a-2h show the mean rotational KE spectra $[K^\psi(k)]$ and the ratio of divergent to rotational KE spectra $[K^\phi(k)/K^\psi(k)]$ for summer and winter seasons in different geographic regions. In agreement with previous studies (Rocha, Gille, et al., 2016; Uchida et al., 2017), the spectral slopes in rotational KE spectra in the upper-ocean show

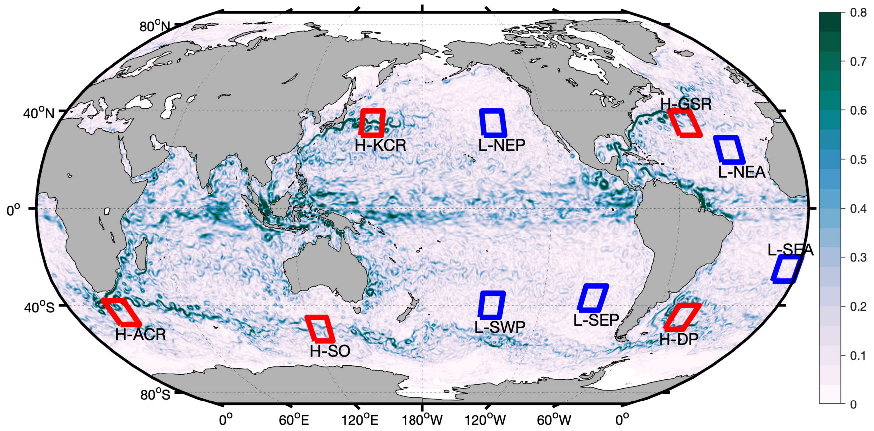

Figure 1. Ten 10° × 10° regions chosen for the spectral analysis. High KE regions (acronyms start with 'H') are shown with red rectangles while blue rectangles represent relatively low KE regions (acronyms start with 'L'). Ocean surface geostrophic speed (m/s) on 15^{th} March 2012 from satellite altimetry dataset is shown in color.

seasonal variability (Figures 2a-2d). The rotational KE spectra (at 21 m depth) in winter are shallower than in summer, whereby they follow a power-law scaling close to k^{-2} at 10-100 km length scales in winter and k^{-3} in summer. This seasonal variability is due to the seasonal strengthening of submesoscale activity in the upper ocean, with submesoscale KE and vorticity magnitudes peaking in the winter season (Dong et al., 2020; Rocha, Gille, et al., 2016; Sasaki et al., 2017).

As seen in Figures 2e-2h, the ageostrophic (divergent) contributions in the upper-ocean can be as large as the geostrophic (rotational) ones within the submesoscale range, especially in the summer season and in low KE regions. Nevertheless, in the winter season, upper ocean submesoscale flows are predominantly rotational, which indicates that they are in near geostrophic balance. Note that rotational and geostrophic spectra are not necessarily equivalent due to the presence of weak vertical velocities associated with the balanced flow (Wang & Bühler, 2020). However, we expect the correction to be insignificant in the upper ocean because $K^{\phi}(k)/K^{\psi}(k)$ is mostly smaller than 1, especially in winter (Figures 2e-2h). Thus, this technical distinction is not important for the analysis presented in this paper. In the following, we consider just the rotational KE spectra as we are interested in geostrophic turbulence.

3.1 Wintertime KE spectra and associated spectral scaling

In the summer, k^{-3} power-law in KE spectra at mesoscales and submesoscales agrees with QG turbulence (Charney, 1971). On the other hand, k^{-2} scaling in winter KE spectra can be understood, in part, in terms of surface-QG dynamics (Blumen, 1978; Klein et al., 2008; Lapeyre, 2009), in which surface buoyancy drives the dynamics. Importantly,

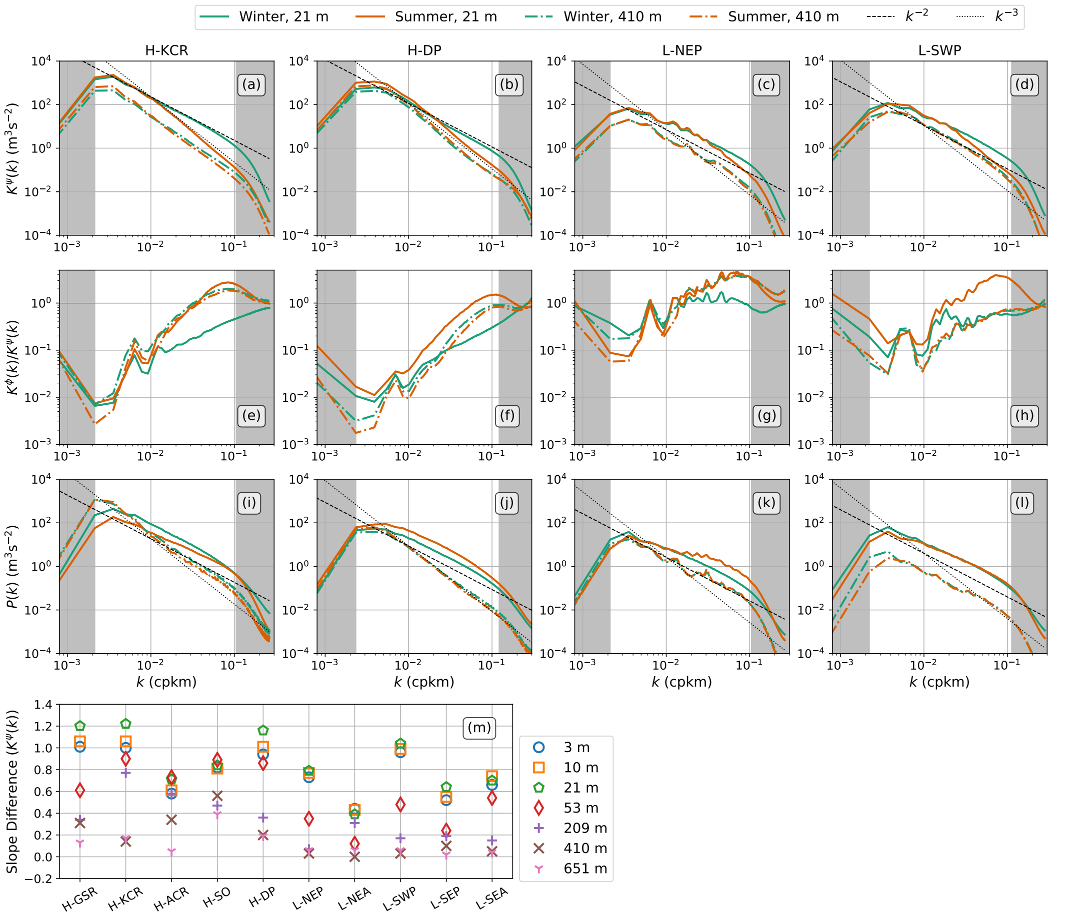

Figure 2. Seasonally-averaged (JJA and DJF) (a-d) rotational KE spectra, (e-f) the ratio of divergent to rotational KE spectra, and (i-l): PE spectra. Each is shown versus isotropic horizontal wavenumber $k = \sqrt{k_x^2 + k_y^2}$ (cycles/km) in selected high and low KE regions at depths of 21 m and 410 m. Gray patches indicate the wavenumbers over which boundary effects (low wavenumbers) and viscous dissipation (high wavenumbers) alter the spectra significantly and so are outside our scope. (m) The differences between the summer and winter spectral slopes (linear fits were computed in the wavenumber range [0.02, 0.06] cpkm) for rotational KE spectra.

the k^{-2} power-law in the winter KE spectra is steeper than the surface-QG prediction of $k^{-5/3}$ in the buoyancy-variance cascading inertial range (Blumen, 1978). With the inclusion of sharp fronts and filaments in surface-QG dynamics (referred to as frontal-surface-QG dynamics here), KE spectra are expected to fall as k^{-2} (Boyd, 1992; Callies & Ferrari, 2013). Thus, the enhanced wintertime submesoscale turbulence and associated k^{-2} scaling in KE spectra agree with frontal-surface-QG dynamics.

Alternatively, the relatively shallow k^{-2} scaling in the mesoscale KE spectra in winter can also arise from an upscale KE transfer due to mixed-layer instabilities, in which perturbations grow by extracting PE from lateral buoyancy gradients (Boccaletti et al., 2007; Callies et al., 2016; Capet, McWilliams, et al., 2008b). In this case, the spectral slope in the KE spectrum at scales larger than the mixed-layer deformation scale is expected to be controlled by two processes: an upscale KE transfer due to mixed-layer instabilities (Boccaletti et al., 2007) and a forward enstrophy transfer due to interior baroclinic instability (Charney, 1971). The QG theory predicts a $k^{-5/3}$ power-law for the KE spectrum in the inverse KE cascade and k^{-3} power-law in the forward enstrophy cascade inertial ranges, respectively (Charney, 1971). Thus, the simulated KE spectral slope of roughly k^{-2} could also be the result of an overlap of these two cascades in wintertime submesoscale KE spectra.

In winter, we expect KE production at two distinct length scales: baroclinic Rossby deformation scale and mixed-layer deformation scale. Lilly (1989) first proposed to study geostrophic turbulence in the presence of two forcing length scales, and this approach may be useful in understanding the nature of upper ocean turbulence. Further, at scales smaller than the mixed-layer deformation scale, a downscale buoyancy variance flux can affect the spectral slope significantly as in surface-QG dynamics. In a recent work, Dong et al. (2020) argued that both the inverse KE transfer and forward buoyancy variance transfer contribute to shaping the k^{-2} scaling in submesoscale KE spectra. However, there is no clarity on the relative importance of the two processes nor on the evolution of KE spectra from summer to winter. We provide insight into these issues in section 4.

3.2 Spectra in the ocean interior

Thus far we have focused on the upper ocean spectra at 21 m depth. For comparison, in Figures 2a-2d we also show the mean rotational KE spectra at 410 m depth. Little seasonal variability is seen at this interior depth. In Figure 2m, we show the differences between the summer and winter spectral slopes (computed in the submesoscale wavenumber range [0.02, 0.06] cpkm) in rotational KE spectra as a function of depth. The seasonal variability is pronounced in the upper 50 m, where the slope differences are close to 1, and can be associated with the seasonality in the mixed layer depth, which varies between 10-20 m in summer and 100-150 m in winter (de Boyer Montégut et al., 2004). For completeness, we also assess seasonally-averaged PE spectra ($P(k)$ in Figure 2i-2l, see supporting information for computational details), which do not indicate any seasonal variability in spectral slopes. However, spectral slope magnitudes can differ between the ocean surface and ocean interior (Callies & Ferrari, 2013; Callies et al., 2016).

4 Interplay among QG turbulence, frontal-surface-QG turbulence, and mixed-layer instabilities

Here, we examine how the upper ocean KE spectra evolve from summer to winter. In Figure 3a, monthly-averaged rotational KE spectra for July, November, and March are shown in the Kuroshio Current region (H–KCR). As discussed in Section 3, the KE spectra follow close to k^{-3} scaling in July whereas the scaling is close to k^{-2} in March due to enhanced submesoscale activity. In the transition month of November, the KE spectrum shows both spectral scalings, with k^{-3} at length scales larger than about 40 km and k^{-2} at smaller length scales.

4.1 Interpreting the dual power-laws

The presence of dual power-laws in the November KE spectrum indicates the coexistence of QG and frontal-surface-QG turbulence. Tulloch and Smith (2006, 2009) incorporated both interior and boundary dynamics in a QG model and showed that the surface KE spectrum follows a k^{-3} power-law at large scales, in agreement with QG theory, and the spectrum transitions to a $k^{-5/3}$ power-law at relatively small scales, in accord with the traditional surface-QG theory. With the consideration of sharp fronts in surface-QG dynamics (Boyd, 1992; Callies & Ferrari, 2013), we expect a change in spectral scaling from k^{-3} at large scales to k^{-2} at relatively small scales in the upper ocean geostrophic KE spectra, and this change in power-law is clearly seen in the November KE spectrum (Figure 3a). Hence, k^{-3} scaling is associated with the downscale enstrophy flux, and k^{-2} spectral scaling is associated with the downscale buoyancy variance flux and ocean fronts (Tulloch & Smith, 2006; Callies & Ferrari, 2013).

Frontal activity is expected to strengthen in late autumn (Kazmin & Rienecker, 1996; Roden, 1980) and the length scale corresponding to the change in spectral scaling (k^{-3} to k^{-2}) may be associated with the frontogenesis scale at which lateral buoyancy gradients are strong. The time series of available PE (APE) in Figure 3b confirms that buoyancy anomalies strengthen in late autumn due to frontogenesis at submesoscales (McWilliams et al., 2015). APE peaks in late autumn and this APE slowly decays by March-April due to mixed-layer instabilities, leading to an increase in the mean enstrophy in late winter (Figure 3c). It is expected that this conversion of APE to KE at submesoscales results in an inverse KE cascade. Consequently, relatively shallow k^{-2} spectral scaling develops in the March KE spectrum, even at length scales as large as 100 km (see discussions in Dong et al., 2020; Sasaki et al., 2017).

As discussed in section 3, the spectral slope in the geostrophic KE spectrum throughout the mesoscales and submesoscales is expected to be controlled by an inverse KE flux (due to mixed-layer instabilities), forward enstrophy flux (due to interior baroclinic instability), and forward buoyancy variance flux (due to frontogenesis). The temporal evolution of KE spectral slope, APE, and enstrophy in Figures 3a-3c confirms the roles of these spectral fluxes in different months. In late winter, instabilities occur at a range of length scales and all three spectral fluxes contribute to shaping the KE spectral slope (also see Dong et al., 2020). Hence, we do not expect an inertial range at 10-100 km scales in late winter, and a theoretical power-law scaling for the KE spectrum is not possible. The appearance of k^{-2} power-law in late winter KE spectra could be a mere coincidence. Nevertheless, the flattening of the KE spectrum in winter is expected due to the inverse KE transfer from mixed-layer instabilities and is robust across the oceanic regions we analyzed.

The presence of dual power-laws in late autumn is also seen in other oceanic regions (Figures 3d-3m), especially in high KE regions. In contrast, there is no clear signature of dual spectral regimes in low KE regions. It has been suggested that seasonal variability in low KE regions is due to seasonality in the KE production rate associated with interior baroclinic instability (Sasaki et al., 2017), which could be a reason for the absence of two spectral regimes in low KE regions.

4.2 Estimating the transition wavenumber

It is natural to ask what sets the transition wavenumber between k^{-3} and k^{-2} scaling in the rotational KE spectrum in late autumn. Here, we derive an expression for predicting the transition wavenumber. In inertial ranges corresponding to downscale enstrophy and buoyancy variance cascades, QG and surface-QG turbulence theories predict the following KE spectra,

$$E_{qg}(k) = C_1 \mathcal{Z}^{2/3} k^{-3} \qquad \text{and} \qquad E_{sqg}(k) = C_2 \mathcal{B}^{2/3} k^{-5/3}. \tag{1}$$

Here, C_1, C_2 are constants, $\mathcal{Z}$ is the enstrophy flux, $\mathcal{B}$ is the buoyancy variance flux divided by the squared buoyancy frequency, $N^2 = -(g/\rho_o)\,\mathrm{d}\rho(z)/\mathrm{d}z$, where $\rho(z)$ is the mean vertical potential density profile (referenced to the sea surface) evaluated using the equation of state from Jackett and Mcdougall (1995). We hypothesize that both QG and surface-QG dynamics determine the geostrophic KE spectral slope (see discussions in Tulloch & Smith, 2009; Tung & Orlando, 2003) and that we can furthermore write $K^{\psi}(k)$ as a linear superposition of $E_{qg}(k)$ and $E_{sqg}(k)$ (Gkioulekas & Tung, 2007a)

$$K^{\psi}(k) = C_1 \mathcal{Z}^{2/3} k^{-3} + C_2 \mathcal{B}^{2/3} k^{-5/3}. \tag{2}$$

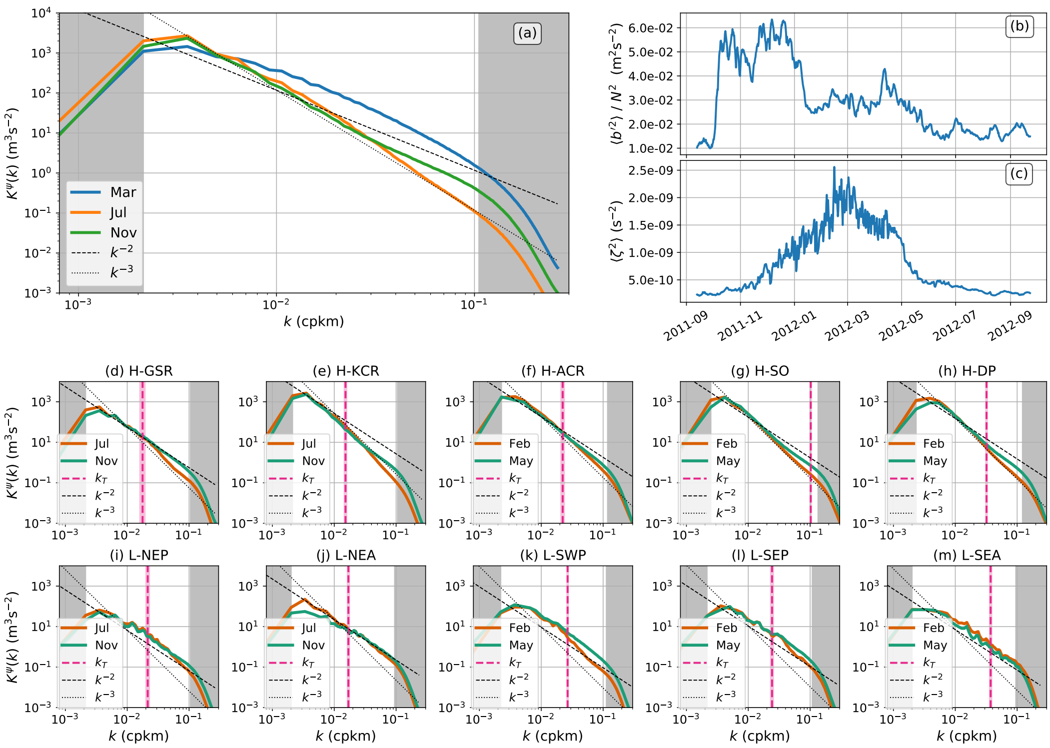

Figure 3. Panels (a-c) results at 21 m depth in the Kuroshio Current region (H-KCR) (a) monthly-averaged rotational KE spectra, (b) domain-averaged APE time series, (c) domain-averaged enstrophy time series. Panels (d-m) monthly-averaged rotational KE spectra in different regions at 21 m depth. Each is shown versus isotropic horizontal wavenumber $k = \sqrt{k_x^2 + k_y^2}$ (cycles/km) and k_T is the transition wavenumber computed using equation (4). November data was used in (d, e, i, j) and May data was used in (f-h, k-m) for computing k_T (shading represents the standard deviation in k_T).

By equating the two terms on the right hand side we obtain the following expression for the transition wavenumber

$$k_T = \left[\frac{C_1}{C_2}\right]^{3/4} \sqrt{\frac{\mathcal{Z}}{\mathcal{B}}}. \tag{3}$$

It is evident that $K^{\psi}(k)$ follows k^{-3} scaling at $k < k_T$ and $k^{-5/3}$ scaling at $k > k_T$. Further, we assume that the spectral flux magnitudes scale with the domain-averaged enstrophy and buoyancy variance. With this assumption, k_T (marked by vertical magenta lines in Figure 3) can be written as

$$k_T \approx \sqrt{\frac{N^2\langle\zeta^2\rangle}{\langle b^2\rangle}}, \tag{4}$$

where $b = -g(\rho - \rho_o)/\rho_o$ is the buoyancy ($g = 9.8$ m/s^2), ζ is the vertical component of the relative vorticity, $\langle . \rangle$ is the spatial mean at a given depth, and we set $C_1 = C_2$.

As seen in Figure 3, the transition wavenumber estimates lie in the range 30-50 km (computed using the data in November and May in regions located in the Northern and Southern hemisphere, respectively) and are close to the wavenumbers at which a change in spectral scaling is found. The H–SO region is an exception and the discrepancy could be due to the formation of deep submesoscale fronts in the Southern Ocean (Siegelman, 2020). KE spectra shown in Figure 3 were computed using the velocity field at 21 m depth but the presence of two spectral regimes is also seen at other depths (see supporting information). Note that in our k_T computations, spatial linear trends were removed from buoyancy and vorticity fields to avoid complications arising from domain-scale north-south temperature gradients. We emphasize that the k_T estimate in equation (4) suffers from the many limitations of scaling arguments. In particular, $C_1 = C_2$ need not hold and spectral flux magnitudes, which we assumed to be constant, generally vary as a function of wavenumber (Khatri et al., 2018). Moreover, we do not account for the presence of fronts.

In Figure 3, we note a time lag of about two months between APE and enstrophy peaks (a time lag is also present in other regions, see supporting information). Dong et al. (2020) observed a similar time lag between the mixed-layer depth maximum and submesoscale KE maximum. So although strong lateral buoyancy gradients are created in late autumn and result in a significant increase in APE, mixed-layer instabilities peak around late winter. This time lag is the key reason why we find two spectral regimes in Figure 3. Equation (4) inherently assumes that domain-averaged enstrophy and buoyancy variance are independent and do not affect each other, which is not expected to hold at all times. As seen in Figure 3, mixed-layer baroclinic instabilities convert APE into KE, which reduces buoyancy variance and increases enstrophy. Nevertheless, the k_T estimate works well in late autumn as mixed-layer instabilities are not as active.

Our analysis suggests that the temporal evolution of upper ocean submesoscale turbulence can be divided into two phases. In the first phase (late autumn), frontogenesis processes create strong lateral buoyancy gradients resulting in two spectral regimes (k^{-3} and k^{-2}) in the geostrophic KE spectrum. In the second phase (late winter), mixed-layer baroclinic instabilities convert APE into KE at submesoscales, and KE cascades upscale leading to a relatively shallow k^{-2} scaling in the KE spectrum at scales as large as 100 km. We provide a schematic in Figure 4 explaining the two phases. Also, k_T estimates in Figure 3 are quite close to the most unstable mixed-layer instability length scales (Figure 1 in Sasaki et al., 2017). This similarity in length scales is expected since submesoscale front length scales and mixed-layer instability scales generally overlap (Hosegood et al., 2006).

5 Discussion and Conclusions

In this study, we used output from a 1/48° global ocean simulation to examine the behavior of upper ocean geostrophic turbulence in different parts of the World Ocean. In agreement with previous studies, we found a strong seasonality in submesoscale turbulence and the associated geostrophic kinetic energy (KE) spectra (Callies et al., 2015; Rocha, Gille, et al., 2016; Sasaki et al., 2017). Specifically, rotational KE spectra tend to follow $\sim k^{-3}$ power-law in summer in accord with QG turbulence (Charney, 1971), and $\sim k^{-2}$ power-law in winter. It is shown that mesoscale and submesoscale turbulence in the upper ocean geostrophic flows can be understood as a combination of quasi-geostrophic (QG), surface-QG, and frontal dynamics.

We described two distinct physical phases in the seasonal transition of upper ocean rotational KE spectra from k^{-3} scaling in summer to k^{-2} scaling in winter. The first phase occurs in late autumn, during which strong lateral buoyancy gradients are created due to frontogenesis at submesoscales (McWilliams et al., 2015). As a result, KE spectra develop two spectral regimes consistent with the coexistence of QG and surface-QG-like turbulence (Tulloch & Smith, 2006, 2009). Specifically, KE spectra decay as k^{-3} at length scales > 50 km associated with the forward enstrophy cascade in QG turbulence (Charney, 1971), whereas KE spectra follow k^{-2} spectral scaling at length scales < 50 km in agreement with the forward buoyancy variance cascade in surface-QG turbulence and the pres-

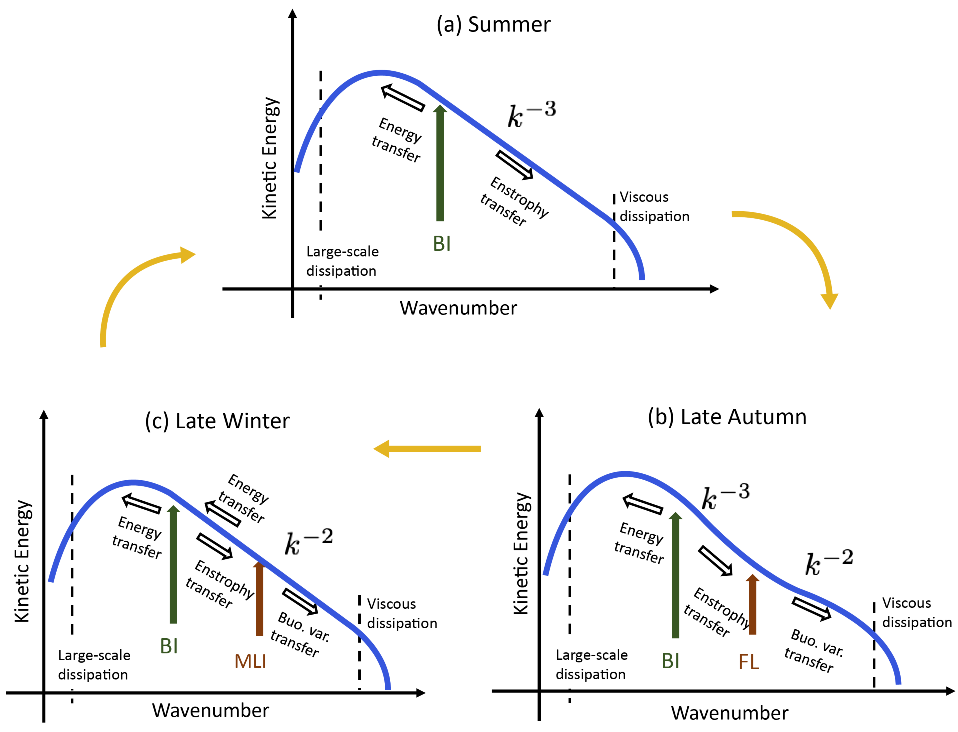

Figure 4. Schematic for the annual cycle of the geostrophic KE spectrum in the upper ocean. (a) From QG turbulence, the summer KE spectrum follows k^{-3} scaling associated with a downscale enstrophy cascade in scales smaller than baroclinic instability length scale (BI) and an inverse KE cascade is present at larger scales. (b) In late autumn, strong lateral buoyancy gradients are created due to frontogenesis (FL indicates the length scale where transition in spectral slope occurs due to the presence of fronts) and buoyancy variance cascades downscale leading to flattening of the KE spectrum to k^{-2} in submesoscales in accord with surface-QG turbulence plus frontal activity. (c) Mixed-layer baroclinic instabilities (MLI indicates the corresponding length scale) extract energy from lateral buoyancy gradients resulting in an upscale cascade of KE. Consequently, both upscale KE flux and downscale enstrophy flux affect the spectral slope, and a shallower $\sim k^{-2}$ scaling develops in the mesoscale KE spectrum. Black arrows denote the directions of the spectral fluxes of KE, enstrophy, and buoyancy variance (note that dimensions of these fluxes are different from each other).

ence of frontal structures (Blumen, 1978; Callies & Ferrari, 2013). Using the mean enstrophy and buoyancy variance magnitudes, we derived a scaling estimate for the wavenumber where the spectral scaling transitions from k^{-3} to k^{-2}. The estimated wavenumbers are able to predict the change in spectral scaling in KE spectra reasonably well. Also, available potential energy (APE) peaks during this time as strong lateral buoyancy gradients are present.

In the second phase, which peaks in late winter, mixed-layer baroclinic instabilities convert APE into KE at submesoscales, thus leading to an inverse KE cascade (see also Dong et al., 2020; Sasaki et al., 2017). Consequently, k^{-2} spectral scaling develops in KE spectra at scales of 10-100 km. We present a schematic in Figure 4 that summarizes the physical mechanisms involved with these seasonal transitions, thus depicting our finding that geostrophic turbulence in the upper ocean can be understood in terms of QG, surface-QG, and frontal dynamics, with the relative importance of these processes varying seasonally.

Another key finding of this work is that a time lag of about 2-3 months occurs between the maxima in APE due to frontogenesis and its conversion to submesoscale KE through mixed-layer baroclinic instabilities (also see Dong et al., 2020). Although frontogenesis processes start in late autumn, mixed-layer baroclinic instabilities peak in late winter. Current submesoscale mixed-layer parameterization schemes do not account for this time lag, and APE is converted into KE instantly in the mixed-layer (Fox-Kemper et al., 2008). In practice, however, some ocean models use temporal smoothing to obtain more realistic circulation. For example, the GFDL-OM4 ocean climate model uses 30 days as the time-scale for temporal smoothing (Adcroft et al., 2019). Currently, these time scale magnitudes are tuned to match model output to ocean measurements. However, physical reasoning is missing for this temporal smoothing. We are pursuing research to determine a scaling-argument-based relation for the time scale for use in submesoscale parameterization schemes.

Acknowledgments

The idea of this study originated at the summer school "Fundamental aspects of turbulent flows in climate dynamics" in summer 2017 at École de Physique des Houches, France. Discussions with Jai Sukhatme, Jörn Callies, Raffaele Ferrari, Dhruv Balwada, Brian Arbic, Oliver Bühler, Ryan Abernathey, and Shafer Smith were helpful in this study. The authors thank Elizabeth Yankovsky and Marion Alberty for comments on the manuscript. The authors would like to thank the team maintaining the PANGEO platform (`https://pangeo.io/`), which was used for computations in this work. The authors are grateful to Catherine Raphael for help with Figure 4. LLC4320 simulation data used in this work is available on the ECCO data portal (`https://data.nas.nasa.gov/ecco/data.php`). Hemant Khatri is sponsored through award NA18OAR4320123 from the National Oceanic and Atmospheric Administration, U.S. Department of Commerce. The statements, findings, conclusions, and recommendations are those of the author(s) and do not necessarily reflect the views of the National Oceanic and Atmospheric Administration, or the U.S. Department of Commerce. Dimitris Menemenlis carried out research at the Jet Propulsion Laboratory, California Institute of Technology, under contract with NASA, with support from the Physical Oceanography and Modeling, Analysis, and Prediction Programs. High-End computing was provided by NASA Advanced Supercomputing at Ames Research Center.

References

Adcroft, A., Anderson, W., Balaji, V., Blanton, C., Bushuk, M., Dufour, C. O., . . . others (2019). The gfdl global ocean and sea ice model om4. 0: Model description and simulation features. *Journal of Advances in Modeling Earth Systems*, *11*(10), 3167–3211. doi: 10.1029/2019MS001726

Aluie, H., Hecht, M., & Vallis, G. K. (2017). Mapping the energy cascade in the north atlantic ocean: The coarse-graining approach. *Journal of Physical Oceanography*. doi: 10.1175/JPO-D-17-0100.1

Arbic, B. K., Müller, M., Richman, J. G., Shriver, J. F., Morten, A. J., Scott, R. B., . . . Penduff, T. (2014). Geostrophic turbulence in the frequency–wavenumber domain: Eddy-driven low-frequency variability. *Journal of Physical Oceanography*, *44*(8), 2050–2069. doi: 10.1175/JPO-D-13-054.1

Badin, G. (2013). Surface semi-geostrophic dynamics in the ocean. *Geophysical & Astrophysical Fluid Dynamics*, *107*(5), 526–540. doi: 10.1080/03091929.2012.740479

Blumen, W. (1978). Uniform potential vorticity flow: Part i. theory of wave inter-

actions and two-dimensional turbulence. *Journal of the Atmospheric Sciences*, *35*(5), 774–783. doi: 10.1175/1520-0469(1978)035⟨0774:UPVFPI⟩2.0.CO;2
Boccaletti, G., Ferrari, R., & Fox-Kemper, B. (2007). Mixed layer instabilities and restratification. *Journal of Physical Oceanography*, *37*(9), 2228–2250. doi: 10.1175/JPO3101.1
Boyd, J. P. (1992). The energy spectrum of fronts: Time evolution of shocks in burgers' equation. *Journal of the Atmospheric Sciences*, *49*(2), 128–139. doi: 10.1175/1520-0469(1992)049⟨0128:TESOFT⟩2.0.CO;2
Bühler, O., Callies, J., & Ferrari, R. (2014). Wave-vortex decomposition of one-dimensional ship-track data. *Journal of Fluid Mechanics*, *756*, 1007-1026. doi: 10.1017/jfm.2014.488
Callies, J., & Ferrari, R. (2013). Interpreting energy and tracer spectra of upper-ocean turbulence in the submesoscale range (1–200 km). *Journal of Physical Oceanography*, *43*(11), 2456–2474. doi: 10.1175/JPO-D-13-063.1
Callies, J., Ferrari, R., Klymak, J. M., & Gula, J. (2015). Seasonality in submesoscale turbulence. *Nature Communications*, *6*. doi: 10.1038/ncomms7862
Callies, J., Flierl, G., Ferrari, R., & Fox-Kemper, B. (2016). The role of mixed-layer instabilities in submesoscale turbulence. *Journal of Fluid Mechanics*, *788*, 5–41. doi: 10.1017/jfm.2015.700
Capet, X., Klein, P., Hua, B. L., Lapeyre, G., & Mcwilliams, J. C. (2008). Surface kinetic energy transfer in surface quasi-geostrophic flows. *Journal of Fluid Mechanics*, *604*, 165–174. doi: 10.1017/S0022112008001110
Capet, X., McWilliams, J. C., Molemaker, M. J., & Shchepetkin, A. (2008a). Mesoscale to submesoscale transition in the california current system. part i: Flow structure, eddy flux, and observational tests. *Journal of Physical Oceanography*, *38*(1), 29–43. doi: 10.1175/2007JPO3671.1
Capet, X., McWilliams, J. C., Molemaker, M. J., & Shchepetkin, A. (2008b). Mesoscale to submesoscale transition in the california current system. part iii: Energy balance and flux. *Journal of Physical Oceanography*, *38*(10), 2256–2269. doi: 10.1175/2008JPO3810.1
Charney, J. (1971). Geostrophic turbulence. *Journal of the Atmospheric Sciences*, *28*, 1087–1095. doi: 10.1175/1520-0469(1971)028⟨1087:GT⟩2.0.CO;2
Chereskin, T. K., Rocha, C. B., Gille, S. T., Menemenlis, D., & Passaro, M. (2019). Characterizing the transition from balanced to unbalanced motions in the southern california current. *Journal of Geophysical Research: Oceans*, *124*(3), 2088–2109. doi: 10.1029/2018JC014583
de Boyer Montégut, C., Madec, G., Fischer, A. S., Lazar, A., & Iudicone, D. (2004). Mixed layer depth over the global ocean: An examination of profile data and a profile-based climatology. *Journal of Geophysical Research: Oceans*, *109*(C12). doi: 10.1029/2004JC002378
Dong, J., Fox-Kemper, B., Zhang, H., & Dong, C. (2020). The seasonality of submesoscale energy production, content, and cascade. *Geophysical Research Letters*, *47*(6), e2020GL087388. doi: 10.1029/2020GL087388
Fox-Kemper, B., Ferrari, R., & Hallberg, R. (2008). Parameterization of mixed layer eddies. part i: Theory and diagnosis. *Journal of Physical Oceanography*, *38*(6), 1145–1165. doi: 10.1175/2007JPO3792.1
Fu, L.-L., & Ubelmann, C. (2014). On the transition from profile altimeter to swath altimeter for observing global ocean surface topography. *Journal of Atmospheric and Oceanic Technology*, *31*(2), 560–568. doi: 10.1175/JTECH-D-13-00109.1
Garrett, C., & Munk, W. (1975). Space-time scales of internal waves: A progress report. *Journal of Geophysical Research*, *80*(3), 291–297. doi: 10.1029/JC080i003p00291
Gkioulekas, E., & Tung, K. K. (2007a). Is the subdominant part of the energy spectrum due to downscale energy cascade hidden in quasi-geostrophic tur-

bulence? *Discrete & Continuous Dynamical Systems-B*, *7*(2), 293. doi: 10.3934/dcdsb.2007.7.293

Gkioulekas, E., & Tung, K. K. (2007b). A new proof on net upscale energy cascade in two-dimensional and quasi-geostrophic turbulence. *Journal of Fluid Mechanics*, *576*, 173. doi: 10.1017/S0022112006003934

Haine, T. W., & Marshall, J. (1998). Gravitational, symmetric, and baroclinic instability of the ocean mixed layer. *Journal of physical oceanography*, *28*(4), 634–658. doi: 10.1175/1520-0485(1998)028⟨0634:GSABIO⟩2.0.CO;2

Held, I. M., Pierrehumbert, R. T., Garner, S. T., & Swanson, K. L. (1995). Surface quasi-geostrophic dynamics. *Journal of Fluid Mechanics*, *282*, 1–20. doi: 10.1017/S0022112095000012

Hosegood, P., Gregg, M. C., & Alford, M. H. (2006). Sub-mesoscale lateral density structure in the oceanic surface mixed layer. *Geophysical Research Letters*, *33*(22). doi: 10.1029/2006GL026797

Hoskins, B. J., & Bretherton, F. P. (1972). Atmospheric frontogenesis models: Mathematical formulation and solution. *Journal of the Atmospheric Sciences*, *29*(1), 11–37. doi: 10.1175/1520-0469(1972)029⟨0011:AFMMFA⟩2.0.CO;2

Jackett, D. R., & Mcdougall, T. J. (1995). Minimal adjustment of hydrographic profiles to achieve static stability. *Journal of Atmospheric and Oceanic Technology*, *12*(2), 381–389. doi: 10.1175/1520-0426(1995)012⟨0381:MAOHPT⟩2.0.CO;2

Kazmin, A. S., & Rienecker, M. M. (1996). Variability and frontogenesis in the large-scale oceanic frontal zones. *Journal of Geophysical Research: Oceans*, *101*(C1), 907–921. doi: 10.1029/95JC02992

Khatri, H., Sukhatme, J., Kumar, A., & Verma, M. K. (2018). Surface ocean enstrophy, kinetic energy fluxes, and spectra from satellite altimetry. *Journal of Geophysical Research: Oceans*, *123*(5), 3875–3892. doi: 10.1029/2017JC013516

Klein, P., Hua, B. L., Lapeyre, G., Capet, X., Le Gentil, S., & Sasaki, H. (2008). Upper ocean turbulence from high-resolution 3d simulations. *Journal of Physical Oceanography*, *38*(8), 1748–1763. doi: 10.1175/2007JPO3773.1

Kraichnan, R. H. (1967). Inertial ranges in two-dimensional turbulence. *Physics of Fluids*, *10*(7), 1417–1423. doi: 10.1063/1.1762301

Lapeyre, G. (2009). What vertical mode does the altimeter reflect? on the decomposition in baroclinic modes and on a surface-trapped mode. *Journal of Physical Oceanography*, *39*(11), 2857–2874. doi: 10.1175/2009JPO3968.1

Lapeyre, G. (2017). Surface quasi-geostrophy. *Fluids*, *2*(1), 7. doi: 10.3390/fluids2010007

Lilly, D. K. (1989). Two-dimensional turbulence generated by energy sources at two scales. *Journal of the Atmospheric Sciences*, *46*(13), 2026–2030. doi: 10.1175/1520-0469(1989)046⟨2026:TDTGBE⟩2.0.CO;2

Marshall, J., Adcroft, A., Hill, C., Perelman, L., & Heisey, C. (1997). A finite-volume, incompressible navier stokes model for studies of the ocean on parallel computers. *Journal of Geophysical Research: Oceans*, *102*(C3), 5753–5766.

McKechan, D., Robinson, C., & Sathyaprakash, B. S. (2010). A tapering window for time-domain templates and simulated signals in the detection of gravitational waves from coalescing compact binaries. *Classical and Quantum Gravity*, *27*(8), 084020. doi: 10.1088/0264-9381/27/8/084020

McWilliams, J. C. (2016). Submesoscale currents in the ocean. *Proceedings of the Royal Society A: Mathematical, Physical and Engineering Sciences*, *472*(2189), 20160117. doi: 10.1098/rspa.2016.0117

McWilliams, J. C., Gula, J., Molemaker, M. J., Renault, L., & Shchepetkin, A. F. (2015). Filament frontogenesis by boundary layer turbulence. *Journal of Physical Oceanography*, *45*(8), 1988–2005. doi: 10.1175/JPO-D-14-0211.1

Mensa, J. A., Garraffo, Z., Griffa, A., Özgökmen, T. M., Haza, A., & Veneziani, M. (2013). Seasonality of the submesoscale dynamics in the gulf stream region.

Ocean Dynamics, *63*(8), 923–941. doi: 10.1007/s10236-013-0633-1

Pierrehumbert, R., Held, I., & Swanson, K. (1994). Spectra of local and nonlocal two-dimensional turbulence. *Chaos, Solitons & Fractals*, *4*(6), 1111–1116. doi: 10.1016/0960-0779(94)90140-6

Qiu, B., Chen, S., Klein, P., Wang, J., Torres, H., Fu, L.-L., & Menemenlis, D. (2018). Seasonality in transition scale from balanced to unbalanced motions in the world ocean. *Journal of Physical Oceanography*, *48*(3), 591–605. doi: 10.1175/JPO-D-17-0169.1

Ragone, F., & Badin, G. (2016). A study of surface semi-geostrophic turbulence: freely decaying dynamics. *Journal of Fluid Mechanics*, *792*, 740–774. doi: 10.1017/jfm.2016.116

Rocha, C. B., Chereskin, T. K., Gille, S. T., & Menemenlis, D. (2016). Mesoscale to submesoscale wavenumber spectra in drake passage. *Journal of Physical Oceanography*, *46*(2), 601–620. doi: 10.1175/JPO-D-15-0087.1

Rocha, C. B., Gille, S. T., Chereskin, T. K., & Menemenlis, D. (2016). Seasonality of submesoscale dynamics in the kuroshio extension. *Geophysical Research Letters*, *43*(21), 11–304. doi: 10.1002/2016GL071349

Roden, G. I. (1980). On the variability of surface temperature fronts in the western pacific, as detected by satellite. *Journal of Geophysical Research: Oceans*, *85*(C5), 2704–2710. doi: 10.1029/JC085iC05p02704

Sasaki, H., Klein, P., Sasai, Y., & Qiu, B. (2017). Regionality and seasonality of submesoscale and mesoscale turbulence in the north pacific ocean. *Ocean Dynamics*, *67*(9), 1195–1216. doi: 10.1007/s10236-017-1083-y

Schlösser, F., & Eden, C. (2007). Diagnosing the energy cascade in a model of the north atlantic. *Geophysical Research Letters*, *34*(2). (L02604) doi: 10.1029/2006GL027813

Schubert, R., Gula, J., Greatbatch, R. J., Baschek, B., & Biastoch, A. (2020). The submesoscale kinetic energy cascade: Mesoscale absorption of submesoscale mixed layer eddies and frontal downscale fluxes. *Journal of Physical Oceanography*, *50*(9), 2573–2589. doi: 10.1175/JPO-D-19-0311.1

Scott, R. B., & Wang, F. (2005). Direct evidence of an oceanic inverse kinetic energy cascade from satellite altimetry. *Journal of Physical Oceanography*, *35*(9), 1650–1666. doi: 10.1175/JPO2771.1

Siegelman, L. (2020). Energetic submesoscale dynamics in the ocean interior. *Journal of Physical Oceanography*, *50*(3), 727–749. doi: 10.1175/JPO-D-19-0253.1

Sinha, A., Balwada, D., Tarshish, N., & Abernathey, R. (2019). Modulation of lateral transport by submesoscale flows and inertia-gravity waves. *Journal of Advances in Modeling Earth Systems*, *11*(4), 1039–1065. doi: 10.1029/2018MS001508

Su, Z., Wang, J., Klein, P., Thompson, A. F., & Menemenlis, D. (2018). Ocean submesoscales as a key component of the global heat budget. *Nature communications*, *9*(1), 1–8. doi: 10.1038/s41467-018-02983-w

Sukhatme, J., & Pierrehumbert, R. (2002). Surface quasigeostrophic turbulence: The study of an active scalar. *Chaos*, *12*(2), 439–450. doi: 10.1063/1.1480758

Sukhatme, J., & Smith, L. M. (2009). Local and nonlocal dispersive turbulence. *Physics of Fluids*, *21*(5), 056603. doi: 10.1063/1.3141499

Torres, H. S., Klein, P., Menemenlis, D., Qiu, B., Su, Z., Wang, J., … Fu, L.-L. (2018). Partitioning ocean motions into balanced motions and internal gravity waves: A modeling study in anticipation of future space missions. *Journal of Geophysical Research: Oceans*, *123*(11), 8084–8105. doi: 10.1029/2018JC014438

Tulloch, R., Marshall, J., Hill, C., & Smith, K. S. (2011). Scales, growth rates, and spectral fluxes of baroclinic instability in the ocean. *Journal of Physical Oceanography*, *41*(6), 1057–1076. doi: 10.1175/2011JPO4404.1

Tulloch, R., & Smith, K. (2006). A theory for the atmospheric energy spectrum: Depth-limited temperature anomalies at the tropopause. *Proceedings of the National Academy of Sciences*, *103*(40), 14690–14694. doi: 10.1073/pnas.0605494103

Tulloch, R., & Smith, K. S. (2009). Quasigeostrophic turbulence with explicit surface dynamics: Application to the atmospheric energy spectrum. *Journal of the Atmospheric Sciences*, *66*(2), 450–467. doi: 10.1175/2008JAS2653.1

Tung, K. K., & Orlando, W. W. (2003). The k- 3 and k- 5/3 energy spectrum of atmospheric turbulence: Quasigeostrophic two-level model simulation. *Journal of the atmospheric sciences*, *60*(6), 824–835. doi: 10.1175/1520-0469(2003)060⟨0824:TKAKES⟩2.0.CO;2

Uchida, T., Abernathey, R., & Smith, S. (2017). Seasonality of eddy kinetic energy in an eddy permitting global climate model. *Ocean Modeling*, *118*, 41–58. doi: 10.1016/j.ocemod.2017.08.006

Uchida, T., Balwada, D., Abernathey, R., McKinley, G., Smith, S., & Lévy, M. (2019). The contribution of submesoscale over mesoscale eddy iron transport in the open southern ocean. *Journal of Advances in Modeling Earth Systems*, *11*(12), 3934–3958. doi: 10.1029/2019MS001805

Wang, H., & Bühler, O. (2020). Ageostrophic corrections for power spectra and wave–vortex decomposition. *Journal of Fluid Mechanics*, *882*. doi: 10.1017/jfm.2019.815

Wortham, C., & Wunsch, C. (2014). A multidimensional spectral description of ocean variability. *Journal of Physical Oceanography*, *44*(3), 944–966. doi: 10.1175/JPO-D-13-0113.1

Xu, Y., & Fu, L.-L. (2012). The effects of altimeter instrument noise on the estimation of the wavenumber spectrum of sea surface height. *Journal of Physical Oceanography*, *42*(12), 2229–2233. doi: 10.1175/JPO-D-12-0106.1

Supporting Information for "A synthesis of upper ocean geostrophic kinetic energy spectra from a global submesoscale permitting simulation"

Hemant Khatri[1], Stephen M. Griffies[1,2], Takaya Uchida[3], Han Wang[4],

Dimitris Menemenlis[5]

[1]Atmospheric and Oceanic Sciences Program, Princeton University, Princeton, New Jersey, USA

[2]NOAA Geophysical Fluid Dynamics Laboratory, Princeton, New Jersey, USA

[3]Institut des Géosciences de l'Environnment, Centre National de la Recherche Scientifique, Grenoble, France

[4]Department of Physics, University of Toronto, Toronto, Canada

[5]Jet Propulsion Laboratory, California Institute of Technology, Pasadena, California, USA

Contents of this file

1. Text S1 on the details of spectral computations.
2. Text S2 on transition wavenumber estimates.
3. Table S1 on details of the latitude and longitude extent of oceanic regions.
4. Figures S1 shows monthly-averaged geostrophic spectra at 3 m depth.

Corresponding author: Hemant Khatri, Atmospheric and Oceanic Sciences Program, 300 Forrestal Road, Sayre Hall, Princeton, NJ 08540-6654, USA. (hkhatri@princeton.edu)

5. Figure S2 shows the time series of the mean potential energy and enstrophy.

6. Figure S3 shows monthly-averaged rotational kinetic energy and potential energy spectra in late autumn.

Introduction

The document contains additional text, table and figures to support the results presented in the manuscript.

S1. Horizontal wavenumber spectra computations

We follow the methods from Uchida, Abernathey, and Smith (2017) for computing horizontal wavenumber spectra. We compute spectra of kinetic energy (KE) and potential energy (PE) for each model snapshot and used time-averaged spectra for the analysis. In particular, two-dimensional (2D) discrete Fourier transform along both horizontal directions of the velocity and buoyancy fields can be computed first to obtain 2D spectra of KE, $E(k_x, k_y)$, and PE, $P(k_x, k_y)$,

$$E(k_x, k_y) = \frac{1}{2\Delta k_x \Delta k_y} |\tilde{\mathbf{u}}(k_x, k_y)|^2, \tag{1}$$

$$P(k_x, k_y) = \frac{1}{2\Delta k_x \Delta k_y} \frac{|\tilde{b}(k_x, k_y)|^2}{N^2}, \tag{2}$$

where $\mathbf{k} = (k_x,\ k_y)$ is the horizontal wavenumber vector, and $\Delta k_x = 1/(2\Delta x)$, $\Delta k_y = 1/(2\Delta y)$ (Δx and Δy are the zonal and meridional grid spacings) are the inverse of the smallest wavelengths admitted by the model grid. $\tilde{\mathbf{u}}(k_x, k_y)$ and $\tilde{b}(k_x, k_y)$ are the 2D Fourier transform of the velocity and buoyancy ($b = -g(\rho - \rho_o)/\rho_o$, where $g = 9.8$ m/s^2, ρ is the potential density referenced to the ocean surface, $\rho_o = 1000$ kg/m^3 is the reference density). N is the buoyancy frequency ($N^2 = -(g/\rho_o)\,\mathrm{d}\rho(z)/\mathrm{d}z$, where

$\rho(z)$ represents the spatial and time mean vertical potential density profile). Potential density was evaluated using the equation of state from Jackett and Mcdougall (1995). Prior to Fourier transform computations, spatial linear trends were removed from each data snapshot and a 2D Planck-taper windowing function ($\exp[-\frac{0.01}{1-x^2} - \frac{0.01}{1-y^2} + 0.02]$, where $(x, y) \epsilon [-1, 1]$) was used to make the fields doubly-periodic. Planck-taper window is quite effective in reducing signal leakage (McKechan et al., 2010). Alternatively, a Hanning window (or other windowing operations) can be used for this purpose (see e.g. Rocha, Gille, Chereskin, and Menemenlis (2016)).

A Helmholtz decomposition can be used to obtain the KE spectra corresponding to the rotational and divergent components of the horizontal flow (Bühler et al., 2014; Uchida et al., 2017). Decomposing the horizontal velocity, $\mathbf{u}$, in terms of a streamfunction, ψ, and velocity potential, ϕ, yields

$$\mathbf{u} = \mathbf{u}_\psi + \mathbf{u}_\phi = \hat{\mathbf{z}} \times \nabla\psi + \nabla\phi, \tag{3}$$

$$\zeta = \hat{\mathbf{z}} \cdot (\nabla \times \mathbf{u}) = \nabla^2\psi, \tag{4}$$

$$\mathcal{D} = \nabla \cdot \mathbf{u} = \nabla^2\phi, \tag{5}$$

where ζ and $\mathcal{D}$ are the vertical components of the relative vorticity and horizontal divergence, respectively. In Fourier space, the above relations take the form

$$\tilde{\zeta} = -(k_x^2 + k_y^2)\tilde{\psi} \qquad \text{and} \qquad \mathcal{D} = -(k_x^2 + k_y^2)\tilde{\phi}. \tag{6}$$

We can then use these equations to compute rotational (K^ψ) and divergent (K^ϕ) components of the KE spectra ($E = K^\psi + K^\phi$) as

$$K^\psi = \frac{1}{2}|\tilde{\mathbf{u}_\psi}|^2 = \frac{|\tilde{\zeta}|^2}{2(k_x^2 + k_y^2)}, \tag{7}$$

$$K^{\phi} = \frac{1}{2}|\tilde{\mathbf{u}_{\phi}}|^2 = \frac{|\tilde{\mathcal{D}}|^2}{2(k_x^2 + k_y^2)}. \tag{8}$$

In this paper, we azimuthally integrate the 2D spectra to obtain spectra as a function of the isotropic wavenumber, $k = (k_x^2 + k_y^2)^{1/2}$.

S2. Comparing the transition wavenumber estimate against other studies

Tulloch and Smith (2006) studied the coexistence of quasi-geostrophic (QG) and surface-QG turbulence by incorporating both interior and boundary dynamics in an idealized model. They observed the change in spectral scaling from k^{-3} to $k^{-5/3}$ in the surface KE spectrum and defined the corresponding transition wavenumber as $k_T = f/NH$, where f is the Coriolis parameter, N is buoyancy frequency and H is equivalent to thermocline depth.

Our k_T definition in equation (4) in the manuscript agrees with the transition wavenumber estimated by Tulloch and Smith (2006). We see the equivalence by using scaling arguments with $b = f\,\partial\psi/\partial z$ (b is buoyancy and ψ is streamfunction) from geostrophy and $\zeta = k_T^2\psi$ (ζ is the relative vorticity), thus yielding

$$k_T = \frac{f}{NH} = \frac{f}{N}\sqrt{\frac{\langle\psi^2\rangle}{H^2}\frac{1}{\langle\psi^2\rangle}}, \tag{9}$$

$$k_T \approx \frac{f}{N}\sqrt{\langle|\frac{\partial\psi}{\partial z}|^2\rangle\frac{1}{\langle\psi^2\rangle}} \approx \frac{1}{N}\sqrt{\frac{\langle b^2\rangle}{\langle\zeta^2\rangle}k_T^4}, \tag{10}$$

$$k_T \approx \sqrt{\frac{N^2\langle\zeta^2\rangle}{\langle b^2\rangle}}. \tag{11}$$

References

Bühler, O., Callies, J., & Ferrari, R. (2014). Wave-vortex decomposition of one-dimensional ship-track data. *J. Fluid Mech.*, *756*, 1007-1026. doi: 10.1017/jfm.2014.488

Gkioulekas, E., & Tung, K. K. (2007). Is the subdominant part of the energy spectrum due to downscale energy cascade hidden in quasi-geostrophic turbulence? *Discrete & Continuous Dynamical Systems-B*, *7*(2), 293. doi: 10.3934/dcdsb.2007.7.293

Jackett, D. R., & Mcdougall, T. J. (1995). Minimal adjustment of hydrographic profiles to achieve static stability. *Journal of Atmospheric and Oceanic Technology*, *12*(2), 381–389. doi: 10.1175/1520-0426(1995)012⟨0381:MAOHPT⟩2.0.CO;2

McKechan, D., Robinson, C., & Sathyaprakash, B. S. (2010). A tapering window for time-domain templates and simulated signals in the detection of gravitational waves from coalescing compact binaries. *Classical and Quantum Gravity*, *27*(8), 084020. doi: 10.1088/0264-9381/27/8/084020

Rocha, C. B., Gille, S. T., Chereskin, T. K., & Menemenlis, D. (2016). Seasonality of submesoscale dynamics in the kuroshio extension. *Geophysical Research Letters*, *43*(21), 11–304. doi: 10.1002/2016GL071349

Tulloch, R., & Smith, K. (2006). A theory for the atmospheric energy spectrum: Depth-limited temperature anomalies at the tropopause. *Proceedings of the National Academy of Sciences*, *103*(40), 14690–14694. doi: 10.1073/pnas.0605494103

Uchida, T., Abernathey, R., & Smith, S. (2017). Seasonality of eddy kinetic energy in an eddy permitting global climate model. *Ocean Modell.*, *118*, 41–58. doi: 10.1016/j.ocemod.2017.08.006

Table S1. Latitude and longitude bands of different regions. Acronyms for high and relatively low KE regions start with 'H' and 'L', respectively.

Acronyms	Latitudinal Extent	Longitudinal Extent	Location
H–GSR	30°N – 40°N	55°W – 45°W	Gulf Stream Region
H–KCR	30°N – 40°N	150°E – 160°E	Kuroshio Current Region
H–ACR	48°S – 38°S	20°E – 30°E	Agulhus Current Region
H–SO	55°S – 45°S	120°E – 130°E	Southern Ocean
H–DP	50°S – 40°S	50°W – 40°W	Drake Passage Region
L–NEP	30°N – 40°N	150°W – 140°W	North East Pacific
L–NEA	19°N – 29°N	38°W – 28°W	North East Atlantic
L–SWP	45°S – 35°S	150°W – 140°W	South West Pacific
L–SEP	42°S – 32°S	100°W – 90°W	South East Pacific
L–SEA	30°S – 30°S	10°W – 0°W	South East Atlantic

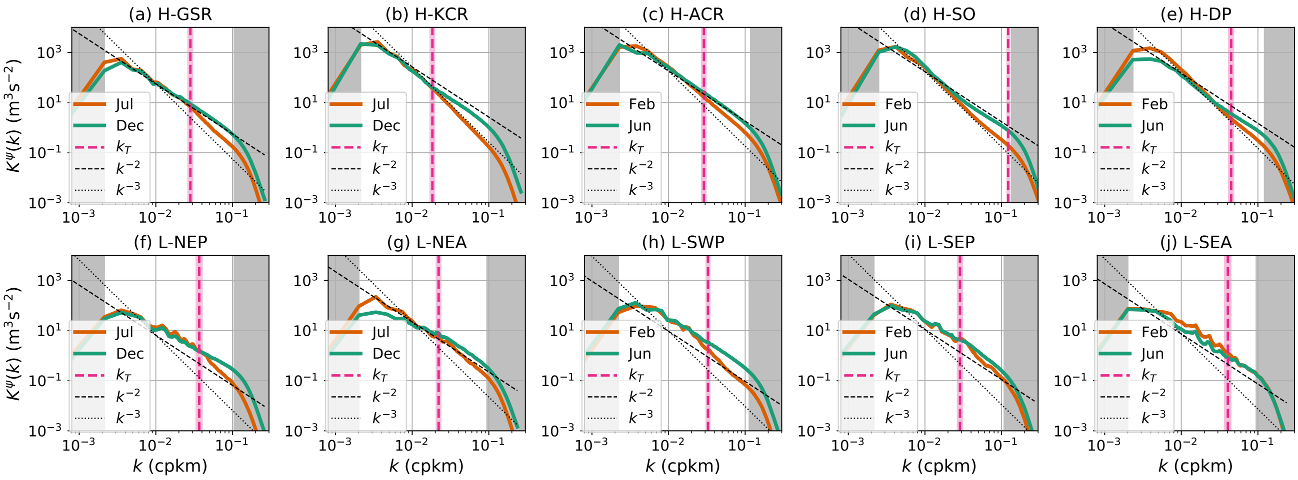

Figure S1. Monthly-averaged rotational KE spectra versus isotropic horizontal wavenumber $k = \sqrt{k_x^2 + k_y^2}$ at 2.79 m depth in different regions. k_T is the transition wavenumber computed using the relation in equation 1 (computed using Dec month data in (a, b, f, g) and June month data in (c-e, h-j)) and shading represents the standard deviation. k^{-2} and k^{-3} curves are shown with dashed and dotted black lines, respectively. Gray regions indicate the wavenumbers over which boundary effects (low wavenumbers) and viscous dissipation (high wavenumbers) significantly alter the spectra, so are outside our scope. Unlike in the manuscript, we show spectra computed for the months of Dec (a, b, f, g) and June (c-e, h-j) because we only computed spectra for DJF and JJA seasons at 2.79 m depth level to limit the computational expense. Nevertheless, dual spectral inertial ranges are evident, which indicates the coexistence of QG turbulence and frontal-surface-QG turbulence.

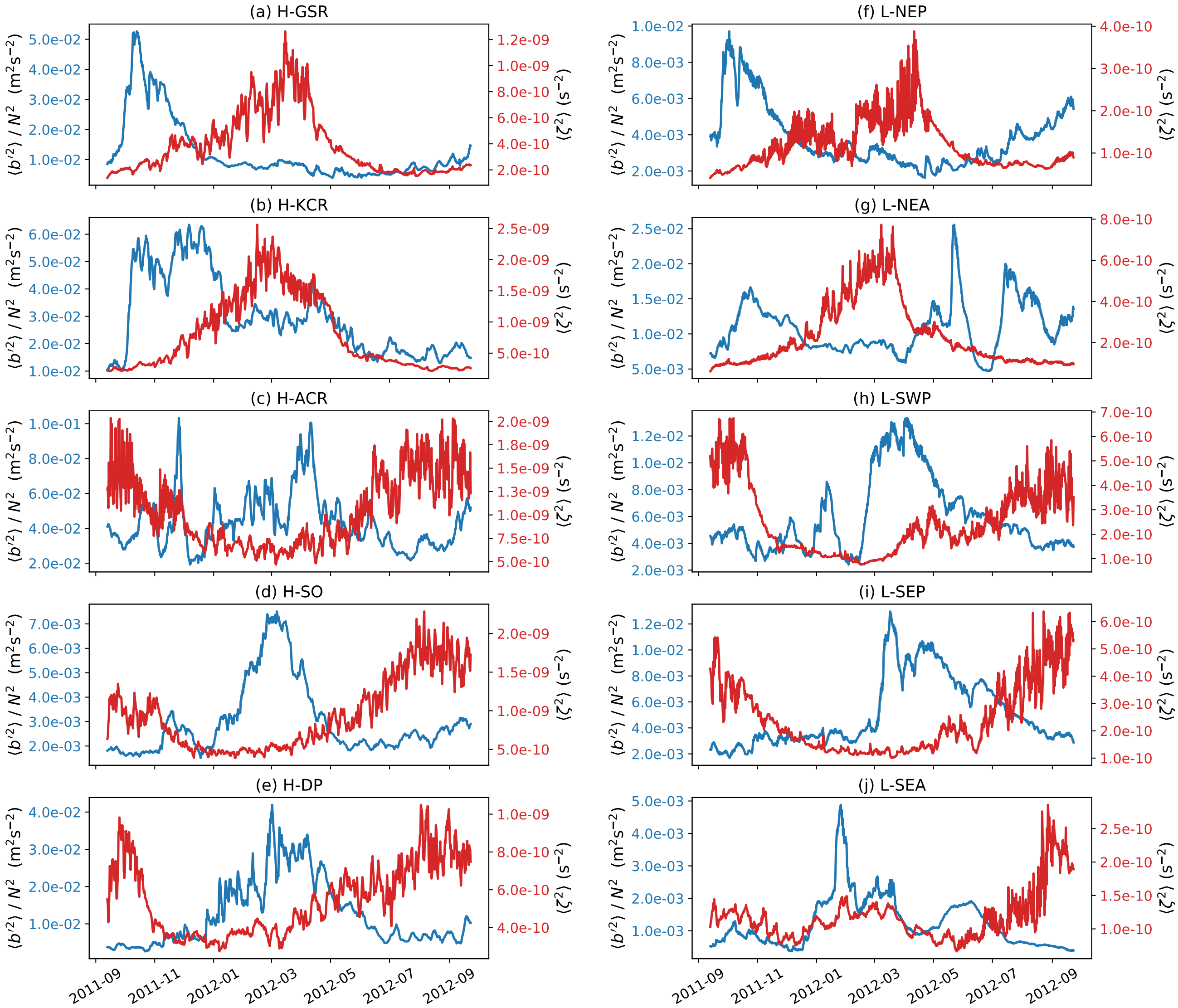

Figure S2. Time series of domain-averaged available potential energy (blue) and domain-averaged enstrophy (red) at 21 m depth in different regions. There is a lag of about 2-4 months in the peaks of available potential energy and enstrophy in all regions.

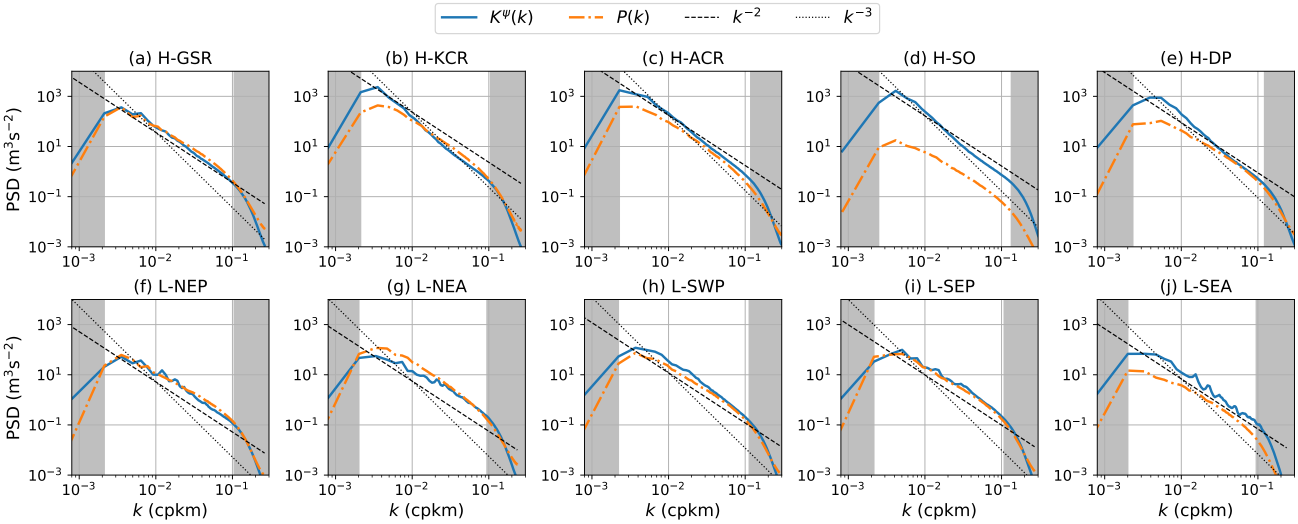

Figure S3. Monthly-averaged rotational kinetic energy ($K^{\psi}(k)$) and potential energy ($P(k)$) spectra in late autumn at 21 m depth in different regions. Spectra shown are for the month of Nov in (a, b, f, g) and for the month of May in (c-e, h-j). k^{-2} and k^{-3} curves are shown with dashed and dotted black lines, respectively. Gray regions indicate the wavenumbers over which boundary effects (low wavenumbers) and viscous dissipation (high wavenumbers) significantly alter the spectra, so are outside our scope. At length scales larger than about 50 km, $K^{\psi}(k)$ follows close to k^{-3} scaling. At length scales smaller than about 50 km, the spectral slope in $K^{\psi}(k)$ is relatively shallow, $\sim k^{-2}$, due to pronounced frontal-surface-QG behavior (see the description of figure 3 in the manuscript). In high KE regions, at these scales (< 50 km), $K^{\psi}(k)$ and $P(k)$ are of similar magnitudes with similar power-law scaling, and this energy equipartition is expected in surface-QG dynamics (Gkioulekas & Tung, 2007). However, the energy equipartition condition is not satisfied in the H–SO region (k_T estimate also does not match the wavenumber corresponding to the spectral scaling change in this region, see manuscript).